ELSEVIER

Journal of Structural Geology 25 (2003) 2125–2139

JOURNAL OF STRUCTURAL GEOLOGY

www.elsevier.com/locate/jsg

Stress field analysis at the El Teniente Mine: evidence for N–S compression in the modern Andes

Stephen D. McKinnon[a,*], Ivan Garrido de la Barra[b]

[a]*Department of Mining Engineering, Queen's University, Kingston, Ontario, Canada K7L 3N6*
[b]*IGB Ltda., Casilla 189, Correo San Enrique, Lo Barnechea, Santiago, Chile*

Accepted 21 March 2003

Abstract

There is a large database of triaxial stress measurements at the El Teniente Mine, Central Chile, but the complex geology, severe topography, and proximity of all measurements to extensive mining excavations made interpretation of the stress field difficult. The measurements were analyzed using three-dimensional numerical stress analysis and decomposition of the stress field into gravitational and tectonic components. By removing gravitational stresses plus local effects from the tectonic component of the stress field a calculation of the far-field tectonic stress tensor is made. It is shown that variations in the tectonic component of stress are related to shear zones cutting through the mine. The far-field major principal component of the tectonic stress field was found to be oriented approximately N–S. This is consistent with the most recent direction of local shortening based on kinematic analysis of faults, but is perpendicular to the direction of regional crustal shortening. There appears to be a limiting envelope to the magnitude of the stress field implying that the shear zones are in a state of limiting equilibrium with regional tectonic driving forces.

Keywords: Stress measurement; Stress analysis; Numerical model; Kinematic analysis; Porphyry copper deposit; Modern Andes

1. Introduction

Numerical stress analysis has been used at the El Teniente Mine, located on the western portion of Central Chile's Andean Cordillera, as a tool to carry out various types of stability assessments. Calibration of the numerical models to in situ stresses was therefore important. For this, use was made of a large database of stress measurements that had been accumulated at the mine over a period of more than 10 years. This database was a good resource for models concerning specific regions of the mine but difficulties were encountered when trying to calibrate three-dimensional mine-scale models. A number of factors led to complications in interpreting the stress measurements, the most important of which were the complex excavation geometry caused by the large extent of mining, severe surface topography, and complex geology. These strong local influences made direct comparison of the measurements practically meaningless.

How does one characterize a stress field in such circumstances? Simple equations relating stress field variations with depth (e.g. Brown and Hoek, 1978; Herget, 1987) are inadequate in mountainous regions. Analytical methods of computing stress field perturbations due to topography (e.g. Savage and Swolfs, 1986; Savage 1993; Pan et al., 1994), or excavations of various shapes (Timoshenko and Goodier, 1970), were too simple to be applied to the El Teniente Mine. The only solution available was to use the numerical models themselves as tools with which to interpret the measurements. This paper describes the database of measurements, how it was analyzed and interpreted, and how the stress field was influenced by geology.

2. Description of the geology

The El Teniente Mine is a world-class copper porphyry deposit located in the Andean segment (Tassara and Yañez, 1997) between 31° and 34° south latitude of the Andes Cordillera, and is characterized by large volumes of hydrothermal breccias, high hypogene grade (>0.8% Cu) and Cu–Mo mineralization (Fig. 1). The geotectonic evolution responsible for the origin of the El Teniente porphyry copper deposit started with a progressive decrease

* Corresponding author. Tel.: +1-613-533-6553; fax: +1-613-533-6597.
E-mail address: sm@mine.queensu.ca (S.D. McKinnon).

0191-8141/03/$ - see front matter © 2003 Elsevier Ltd. All rights reserved.
doi:10.1016/S0191-8141(03)00068-3

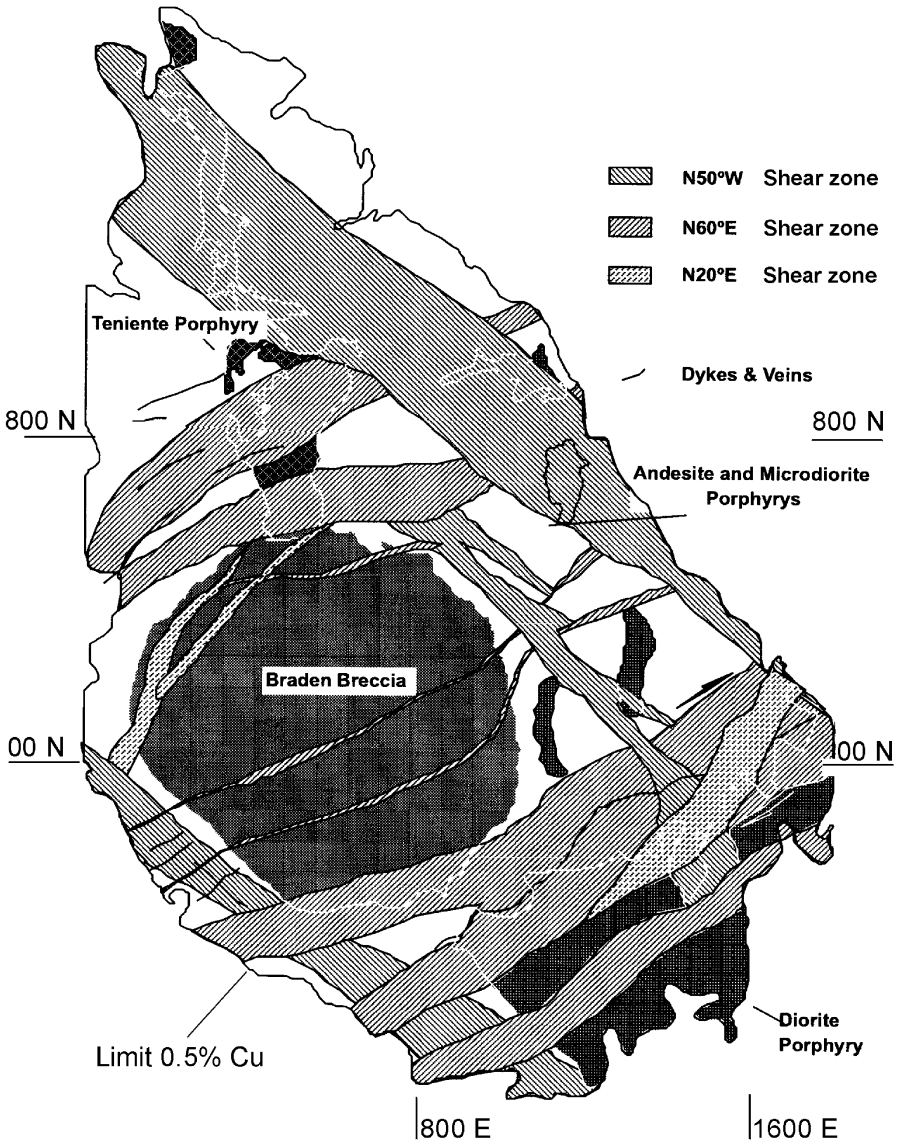

Fig. 1. Map of mine showing main structural features. These include the centrally located volcanic pipe, shear zones and intrusive plutons.

of the Nazca Plate subduction angle. This process may have been triggered by the arrival of the Juan Fernández ridge at these latitudes at ca. 12–10 Ma. This first-order event activated other processes in such a way that crustal thickening and subsequent volcanic arc abandonment followed the bulk E–W shortening associated with subduction shallowing (Garrido et al., 2002).

The most important tectonic feature at the district scale is the ENE-striking, sub-vertical, Teniente fault zone (TFZ). The TFZ is a ca. 10-km-long belt marked by densely faulted, altered and mineralized rock and is characterized by a right-lateral strike-slip movement (Garrido et al., 1994). Immediately east of El Teniente District, the regional-scale structure is dominated by N–S striking thrusts organized into the Aconcagua fold-and-thrust-belt of Miocene age (Ramos et al., 1996). The last tectonic event of the region is a NNE–SSW shortening direction (Lavenu and Cembrano, 1999; Garrido et al., 2002).

Kinematic analysis of the TFZ using the technique of Marrett and Allmendinger (1990) has revealed two episodes of deformation (Garrido et al., 1994). The first episode was contemporary with the intrusion of quartz-diorite to tonalite stocks (5.6 Ma) and northern dacite porphyry (5.2 Ma) that outcrop inside the mine (SHRIMP U–Pb Zircon dating; Maksaev et al., 2002) and resulted in predominantly northwest shortening. This episode was responsible for the formation of the TFZ. The last episode is documented by faults that cut a 3.8 Ma dyke (Postore amphibole-rich andesitic dikes with ^{40}Ar–^{39}Ar date of 3.85 ± 0.18 Ma; Maksaev et al., 2002) and yield an approximately N–S shortening direction.

During the first episode of deformation, strain was accommodated by the formation of many small fractures in the shear zones, each with relatively minor displacement, plus a small number of discrete faults on which larger displacement was accumulated. Neither deformation episode has a direction of shortening corresponding to the

general E–W regional shortening that would be expected based on the convergence directions of the Nazca and South American plates (Garrido et al., 2002).

Records of crustal seismicity in the vicinity of the mine do not indicate that the TFZ is currently active although a lineament of activity with a similar orientation was noted approximately 30 km to the south of the mine. This does not imply that the TFZ is stable and not participating in the ongoing continental deformation. Numerical modeling work by the authors (McKinnon and Garrido de la Barra, 1998), has shown that in regions of confined lithosphere undergoing transpression (a combination of pure and simple shear; see Sanderson and Marchini, 1984), shear zones are not continuously active. Rather, activity at any instant in time may be limited to only a small number of structures, with the location of active structures changing with time to produce distributed strain. Therefore, over geologic time the TFZ may be active even though it may appear to be a dormant feature in the current 'instant' of time covered by the seismic records. The significance of this to the interpretation of the stress measurements is that the stress field in a system close to a state of limiting equilibrium would differ considerably from one in which the structures and stress field are not related. The analysis results were used to examine this possibility.

3. Description of the mine

Mining is predominantly by panel caving with a small amount of standard block caving. Production rates vary between 80 and 85 kt/day of ore with grades of approximately 1.5% Cu, making it the worlds largest underground mine. The upper levels of the orebody have been completely caved and all current mining activity underlies a large subsidence crater. During the time span in which the stress measurements were made, the elevation (sea level datum) of the deepest mining was 2102 m, the Sub-6 level, and the highest level of mining was approximately 2400 m, Teniente-3 Isla. The depth below surface of the active mining levels varies considerably because of the irregular and steep surface topography, but is typically in the range of 450–900 m. To place these distances in perspective, mountain peaks to the east against which the subsidence crater is forming exceed 3600 m elevation and a river valley to the west drops to an elevation of approximately 1900 m. Topography around the mine is therefore significant. A typical cross-section through the mine is shown in Fig. 2. Details of the mining operation and related issues can be found in the literature (Kvapil et al., 1989; Rojas et al., 1992).

Fig. 1 shows a geological map of the mine. The main features of interest to this study are the centrally located Braden Pipe, which is a carrot-shaped volcanic structure devoid of copper mineralization, the diorite and dacite intrusives, and the two predominant sets of shear zones (striking N50°W and N60°E) and associated faults and dikes. Fracture frequencies in the shear zones can exceed $10/m^3$, whereas outside of the shear zones they are typically below $5/m^3$. Although shear zones in Fig. 1 are shown with distinct boundaries, actual boundaries between shear zones and the host rock are gradational and the fractures tend to strike sub-parallel to the shear zone boundaries and have sub-vertical dip. At the intersection of shear zones, the structural patterns are more complex, but in general, the fractures follow the orientations of the two individual shear zones.

4. Description of the stress measurement database

The database of triaxial stress measurements evolved over time in response to a variety of investigations carried out at the mine. As a result, not all measurements were suitable for calibration of the numerical models. Some measurements were made in pillars or other locations where the effects of specific local geometry could not be adequately accounted for in the numerical models. Measurements made close to caving were rejected because of the high probability that they were within the zone influenced by fracturing or irregularities in the cave line geometry, and were therefore unsuitable for use in calibrating an elastic model. From a total of 63 measurements, 13 measurements were considered unsuitable for the various stated reasons and eliminated from the analyses, i.e. only rejection as opposed to acceptance criteria were used. The remaining measurements were located in different rock types and structural settings, the effects of which were examined in the analysis.

The resulting set of 50 measurements, rotated to a common reference frame based on the mine coordinate system of x east, y vertical, z north (a left-handed system), plunge positive down and trend positive clockwise from north, is shown in Table 1. Units of stress throughout are MPa. The sign convention adopted for stresses is that of elasticity in which compression is negative. For convenience, the data have been grouped into regions of similar location, shown in the left-hand column. These regions correspond to distinct areas of mining. The elevation range covered by the measurements was approximately 500 m, but due to the clustering of measurements on only a few levels, most measurements spanned an elevation interval of approximately 350 m. Orientations of measured principal stress axes, plotted on lower hemisphere projections, are shown in Fig. 3. While some general trends in orientations can be seen, it is clear that there is considerable scatter. The variation in principal stress magnitude shows a similar wide scatter (Table 1). Without further analysis to determine the extent of the effects of caving and topography, it was not possible to determine whether there was a single common stress field with the scatter being a result of various locally induced effects, whether there were several distinct domains

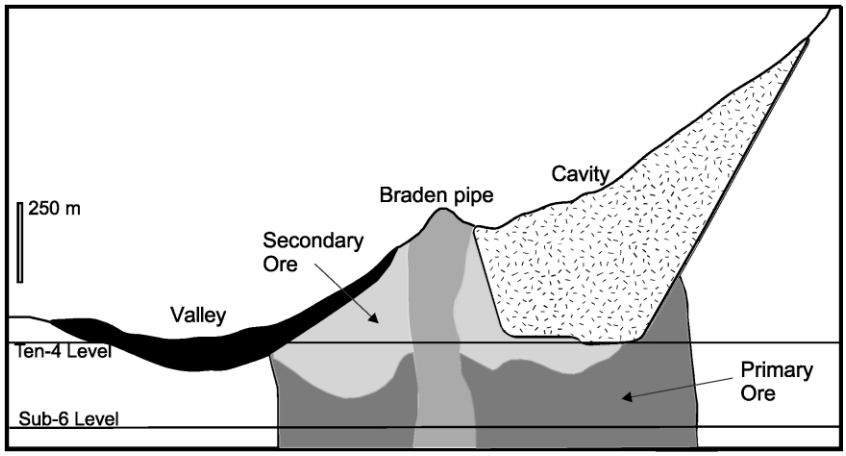

Fig. 2. Cross-section through the orebody, looking north, showing significant topographic relief. The cross section is E–W through the central pipe structure shown in Fig. 1.

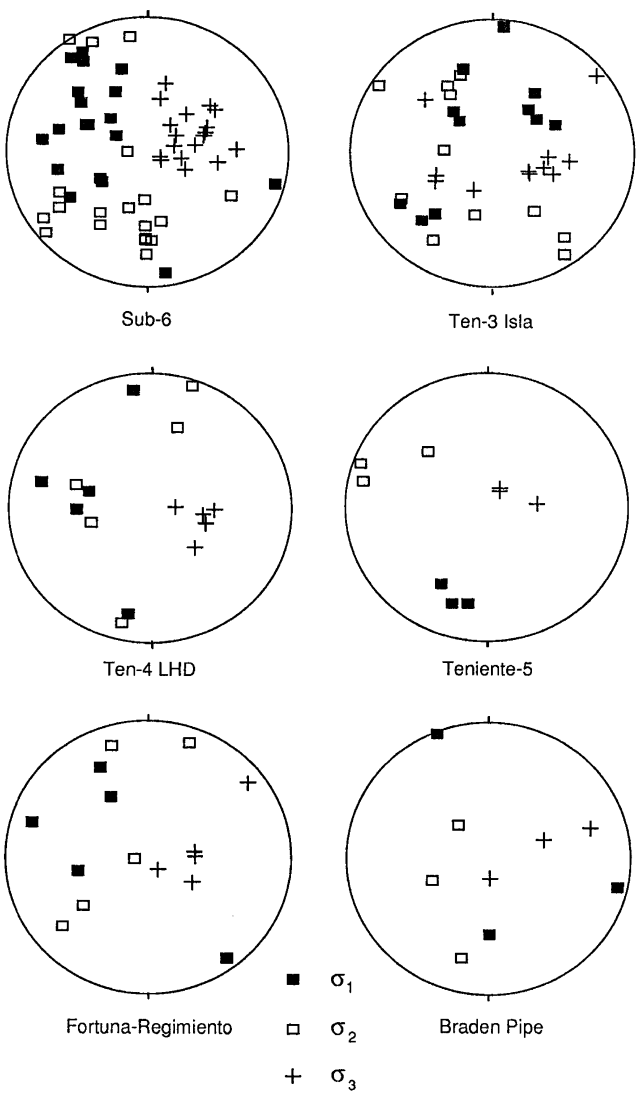

Fig. 3. Lower hemisphere projections (equal angle) of poles of stress measurement principal axes.

of uniform stress, or whether the scatter was simply due to random error in the measurements.

Included in Table 1 is information on the method of measurement. The older measurements utilized either the USBM gage or the CSIR cell (ISRM, 1987) whereas the CSIRO hollow inclusion cell (Duncan Fama and Pender, 1980), has been used since late 1990. All of these instruments measure strain relief in a process of overcoring. The effect of using data obtained using these different methods was not investigated. However, one aspect relevant to interpreting the measurements was a systematic error uncovered by personnel at the mine regarding the Young's modulus values used to convert the measured strains to stresses. In the earlier tests, a sample of rock close to the overcored cell was recovered and the Young's modulus determined in an independent compression test. It was learned that the Young's modulus from these tests was computed from the early loading portion of the stress–strain curve as the samples were not loaded to destruction. This practice resulted in systematically low modulus values and correspondingly higher computed stress magnitudes. After noticing this error, a correction was made, but, uncertainty in the Young's modulus still remained. This source of uncertainty was considered in the method used to analyze the measurements.

5. Data analysis

It was established that conventional methods of analyzing stress measurements would not be effective for the El Teniente environment. This led to the development of a new method, which involved the use of three-dimensional numerical stress analysis. Typically, tractions are specified on the boundaries of numerical models in order to compute the stresses at internal locations that may be influenced by a variety of local geological and geometrical conditions. Depending on the complexity of the problem, the internal

Table 1
Stress measurement data

Location	Date	Site	Method	σ_1	Plunge	Trend	σ_2	Plunge	Trend	σ_3	Plunge	Trend
Sub-6	93	1-2	CSIRO	−23.5	3.6	248.7	−5.8	54.3	343.7	−2.4	35.5	156.2
	93	2-1	CSIRO	−60.0	59.1	299.5	−50.9	15.6	181.7	−23.7	26.0	83.9
	93	2-2	CSIRO	−67.6	25.1	343.7	−40.2	20.6	243.5	−28.6	56.5	118.8
	93	3-1	CSIRO	−72.1	24.7	284.8	−34.9	32.0	178.2	−24.5	47.6	45.1
	93	3-3	CSIRO	−63.9	28.7	307.9	−27.1	51.2	189.9	−14.2	31.2	51.1
	93	4-1	CSIRO	−46.0	25.2	238.4	−40.8	1.1	328.8	−21.7	64.8	61.2
	93	4-2	CSIRO	−34.5	45.9	238.2	−25.2	6.2	334.6	−14.6	43.4	70.5
	93	12-1	CSIRO	−62.0	11.1	326.9	−23.5	7.9	235.3	−12.7	76.3	119.6
	93	12-2	CSIRO	−55.1	8.0	327.8	−25.2	17.3	235.3	−13.6	70.8	81.5
	83	6	USBM	−50.5	24.0	314.0	−27.0	25.0	212.0	−19.5	54.0	82.0
	83	8	USBM	−56.0	8.0	321.0	−50.0	3.0	230.0	−29.5	81.0	120.0
	84	9	USBM	−51.0	16.0	275.0	−36.0	23.0	178.0	−26.0	62.0	36.0
	85	16	USBM	−50.0	7.0	172.0	−48.0	73.0	269.0	−20.5	46.0	74.0
	85	18	CSIR	−60.5	39.0	293.0	−56.0	25.0	181.0	−40.5	41.0	67.0
	85	23	CSIR	−41.0	50.0	313.0	−21.0	14.0	60.0	−16.0	37.0	160.0
	89	39	CSIR	−42.0	36.0	334.0	−36.0	32.0	217.0	−23.5	38.0	98.0
	89	41	CSIR	−50.5	40.0	295.0	−30.5	34.0	170.0	−16.5	32.0	56.0
	90	42	CSIR	−15.5	4.0	105.0	−11.5	42.0	198.0	−11.0	48.0	10.0
	90	43	CSIRO	−87.0	48.0	233.0	−43.6	21.0	119.0	−36.0	35.0	13.0
	90	44	CSIRO	−49.0	25.0	257.0	−28.9	10.0	352.0	−13.9	63.0	101.0
Ten-3	93	7-1	CSIRO	−69.8	54.8	315.6	−32.8	34.9	144.5	−12.2	4.2	51.6
(Isla)	93	8-1	CSIRO	−49.8	22.6	341.5	−44.7	19.6	243.0	−19.6	59.3	116.2
	93	8-2	CSIRO	−36.8	44.9	318.6	−28.5	15.2	212.8	−16.1	41.0	109.0
	93	10-1	CSIRO	−48.8	45.7	50.2	−15.2	4.9	145.3	−9.1	43.8	248.0
	93	10-2	CSIRO	−35.8	37.5	63.4	−16.1	40.8	195.1	−12.5	26.6	310.7
	93	11-1	CSIRO	−53.1	45.8	38.0	−38.6	12.7	141.4	−27.9	41.4	242.9
	93	11-2	CSIRO	−45.8	32.8	34.6	−27.9	3.6	302.2	−18.9	56.9	206.6
	82	3	USBM	−33.5	28.0	220.0	−28.0	30.0	328.0	−15.0	47.0	96.0
	84	11	USBM	−50.0	16.0	240.0	−31.0	27.0	339.0	−24.5	57.0	123.0
	85	20	USBM	−43.0	3.0	5.0	−34.0	53.0	271.0	−25.5	34.0	97.0
	87	27	CSIR	−53.5	19.0	223.0	−37.5	35.0	327.0	−27.0	49.0	110.0
Ten-4	93	9-1	CSIRO	−40.6	41.5	285.3	−26.9	2.7	17.7	−17.2	48.4	110.8
(LHD)	93	9-2	CSIRO	−40.7	34.8	266.9	−29.8	26.3	17.0	−17.3	43.7	135.2
	81	1	USBM	−76.0	2.0	50.0	−45.0	57.0	317.0	−33.0	33.0	141.0
	88	32	CSIR	−37.0	7.0	352.0	−20.0	45.0	256.0	−13.0	44.0	89.0
	88	33	CSIR	−36.0	15.0	284.0	−22.0	9.0	192.0	−13.0	72.0	73.0
	89	37	CSIR	−52.0	13.0	191.0	−29.0	34.0	289.0	−14.0	53.0	83.0
Fortuna/Regi	83	7	USBM	−27.0	18.0	333.0	−21.5	30.0	232.0	−13.0	54.0	90.0
	85	21	USBM	−31.0	36.0	329.0	−24.0	14.0	229.0	−13.5	51.0	122.0
	89	38	CSIR	−41.0	35.0	247.0	−15.5	9.0	343.0	−5.0	54.0	85.0
	91	45	CSIR	−73.5	9.0	288.0	−40.0	7.0	19.0	−37.0	78.0	144.0
	91	46	CSIR	−122.5	5.0	143.0	−67.5	81.0	266.0	−57.0	8.0	52.0
Ten-5	93	5-1	CSIRO	−33.7	23.4	210.1	−20.7	28.9	313.9	−12.4	51.3	87.4
	93	5-2	CSIRO	−31.5	15.8	198.9	−10.7	3.5	289.8	−2.9	73.8	31.9
	93	5-3	CSIRO	−26.1	17.7	189.8	−8.6	6.6	281.9	−1.3	71.1	31.5
Pipe	88	13	CSIRO	−52.0	32.2	178.8	−33.7	53.0	319.4	−23.5	16.3	72.2
	88	14	CSIRO	−40.8	4.3	102.4	−31.8	16.6	193.7	−22.2	72.8	178.3
	88	15	CSIRO	−46.4	1.0	338.7	−29.5	43.9	247.7	−24.1	46.1	69.7
Sub-4	93	6-1	CSIRO	−27.0	28.2	353.5	−17.0	43.2	243.3	−8.9	40.0	101.4
	93	6-2	CSIRO	−66.8	14.3	203.5	−41.1	42.2	306.9	−28.3	44.3	99.1

stress field may differ considerably from that specified on the model boundary. In the stress measurement analysis method developed, the opposite procedure was used, i.e. the locally measured stress field was used to compute the 'far-field' model boundary tractions.

The stress field was divided into gravitational and tectonic stress components. For convenience, all non-gravitational sources of far-field stresses are grouped together in what is referred to as the 'tectonic' component of the stress field. Since the gravitational component of stress must always be present, the problem was one of determining the unknown tectonic component. A stress measurement records the total stress field so we can write:

$$\sigma_{ij}^{\text{meas}} = \sigma_{ij}^{\text{grav}} + \sigma_{ij}^{\text{tect}} \quad (1)$$

The superscript 'meas' refers to the measured stress

tensor, and 'grav' and 'tect' refer to the gravitational and tectonic components of the measured stress tensor, respectively. Since the geometry of the mine excavations and topography are usually well known, as are material densities, it is possible to construct a three-dimensional numerical model and compute the gravitational stress field. The tectonic component of the stress field at the measurement point can then be computed using Eq. (1):

$$\sigma_{ij}^{\text{tect}} = \sigma_{ij}^{\text{meas}} - \sigma_{ij}^{\text{grav}} \tag{2}$$

This estimate includes unknown amounts of mining and topographically-induced stresses. By removing these local effects, we obtain a stress tensor representative of the 'far-field'. Since the gravitational component of the total stress field varies from site to site due to topographic effects, and local influences further complicate the comparison, the far-field tectonic component of the stress field is a particularly useful quantity to compute for comparison purposes. The scheme developed to compute the far-field tectonic stress tensor is described in detail elsewhere (McKinnon, 2001); however, a brief description of the analysis method is provided here, as certain concepts are important for interpretation of the stress measurements.

5.1. Description of analysis method

Assumptions made in the analysis are:

- The stress field is formed entirely by tectonic and gravitational stresses according to Eq. (1).
- The rock mass is linearly elastic and isotropic but not necessarily homogeneous.
- The depth range of measurements is small enough that vertical gradients in the far-field tectonic stresses are ignored.
- In the far field, i.e. at the boundaries of numerical models, the horizontal and vertical stresses are principal stresses.

The objective of the analysis is to determine what boundary tractions must be applied to the numerical model of the mine in order to reproduce the local tectonic stresses of Eq. (2). In the following development, the coordinate system used for the numerically computed stresses is the same as that used for the stress measurements i.e. x east, y vertical and z north. It is convenient, but not essential, that these axes coincide with geographic north and vertical directions.

Using a numerical model of the mine and surrounding surface topography, it is possible to compute the stresses induced at the measurement points due to the application of unit tractions applied to the model boundary. For example, if a unit traction t_x is applied in the x-direction (other lateral boundaries free to deform, and for convenience, model boundaries are taken to be parallel to the coordinate axes), it will induce a state of stress described by the tensor ${}^{\text{m}}\sigma_{ij}^{x}$ at the measurement point. The superscripts m and x refer to stresses sampled at the measurement point in the model due to a unit traction applied in the x-direction on the model boundary. The tensor ${}^{\text{m}}\sigma_{ij}^{x}$ will be referred to as the unit response tensor in the x-direction. This process is illustrated in Fig. 4. Similarly, unit response tensors ${}^{\text{m}}\sigma_{ij}^{z}$ and ${}^{\text{m}}\sigma_{ij}^{xz}$ can be computed using the same model by separately applying unit normal traction t_z and unit shear traction t_{xz}, respectively, on the model boundaries. Note that with this coordinate system, a vertical normal traction t_y applied to the (vertical) model boundary has no physical significance and is not included in the analysis. This also follows from the assumption that in the far field, principal stress axes are vertical and horizontal.

The computed tectonic stress field at the measurement point is assumed to be a linear combination of the three unit response tensors. This assumption is made on the basis that the models are linearly elastic and the total stress field can be computed by superposition of its components:

$${}^{\text{c}}\sigma_{ij}^{\text{tect}} = A\,{}^{\text{m}}\sigma_{ij}^{x} + B\,{}^{\text{m}}\sigma_{ij}^{z} + C\,{}^{\text{m}}\sigma_{ij}^{xz} \tag{3}$$

This is compared with the tectonic component of the stress field estimated from the measurement using Eq. (2). The difference between the two values, Eq. (4), is referred to as the error tensor:

$$\sigma_{ij}^{\text{error}} = D\sigma_{ij}^{\text{meas}} - \sigma_{ij}^{\text{grav}} - (A\,{}^{\text{m}}\sigma_{ij}^{xx} + B\,{}^{\text{m}}\sigma_{ij}^{zz} + C\,{}^{\text{m}}\sigma_{ij}^{xz}) \tag{4}$$

In the analysis of the El Teniente data set the measured stress tensor is scaled by a constant to account for possible Young's modulus errors. This scaling factor is applied to $\sigma_{ij}^{\text{meas}}$ in Eq. (2) and appears as the factor D in Eq. (4). A numerical scheme is used to vary the proportions of the unit response tensors and the measurement tensor in order to minimize the magnitude of the error tensor components.

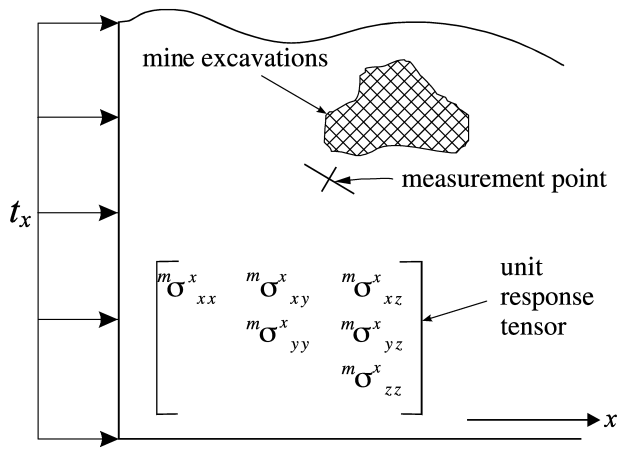

Fig. 4. Definition of unit response tensor, determined at measurement point due to application of unit traction to boundary. Result is a tensor with components as shown, computed at the location in the model corresponding to the measurement point.

The objective function of the minimization process, Ψ, is defined as the sum of the squares of the error tensor components.

$$\Psi = \Sigma(\sigma_{ij}^{\text{error}})^2 \quad (5)$$

Other schemes could be used but the use of least squares resulted in a fairly even distribution of error amongst the error tensor components. This is physically desirable since we have no reason to assume one component of the stress tensor has more error than another.

5.2. Description of the numerical model used in the analysis

The program 3DEC (Itasca, 1994) was used to construct a three-dimensional continuum model of the mine. This program is capable of incorporating discontinuities to represent discrete faults, but since it was not known a priori how the faults would influence the local stress field, none were included in the model. The effect of this assumption is discussed later. Fig. 5 shows two views of the model. Because of the severe topography around the mine, a fairly large lateral extent was chosen to capture enough of the topography that further increases in model size would not affect the computed stresses at the measurement site. Lateral dimensions of the model shown in Fig. 5a are approximately 13 km × 12 km. A view of the caved regions of the mine (full of broken rock), from the southeast looking up, is shown in Fig. 5b. This view spans a distance of approximately 2 km. Since all measurements were located within a few hundred meters at most from any mining, it can be appreciated that the magnitude of mining induced stresses at each site could not be ignored.

As shown in Fig. 1, the rock mass comprises several rock types. Material properties derived from laboratory tests and rock mass classification showed that the lithology could be grouped into six material types, excluding the caved material. The continuum model was therefore cut with vertical boundaries defining regions with different material properties. The location of the boundaries closely followed the structural and lithological boundaries shown in Fig. 1. Material properties were derived using rock mass classification (Hoek and Brown, 1997). The range in estimated rock mass Young's modulus was from 20 to 58 GPa and Poisson's ratio from 0.14 to 0.26. Further details of the properties will not be described as it was found that these material contrasts resulted in only small deviations in the stress field compared with that obtained from a homogeneous material model.

If all measurements had been made at the same time, the unit response tensors and the gravitational stresses at each measurement point could have been determined from a model with a single mining geometry. However, the measurements were made over a time period during which there were significant changes to the mining geometry. Careful examination of the dates of the measurements (see Table 1), plans of the mining sequence, and the locations of the measurements, showed that for modeling purposes the mining geometry at one of three stages, 1988, 1991 and 1993, could be used to represent the geometry at the times when measurements were made. A total of 12 models were therefore used, each with different combinations of mining geometry (three cases) and boundary condition (four cases). The response tensors used in Eq. (4) were extracted from the appropriate model for each measurement point.

5.3. Analysis of individual measurements

The far-field tectonic stress tensor coefficients determined by minimization of Eq. (5) are shown in Table 2. For compactness, only the results for the Sub-6 group of measurements are shown, but results from the entire data set are included in the discussion. The minimization was carried out using the SOLVER function of the Excel 2000 spreadsheet program (Microsoft, 1999). A number of trial starting values for A, B, and C were used in the solution scheme to ensure that the computed minimum error value was not a local minimum reached from a particular starting point. All error values appeared to be global minima.

The scaled measurement analysis resulted in a significant reduction in the magnitude of the error values compared with an unscaled analysis i.e. $D = 1.0$. This did not automatically imply a better fit of the tectonic stress tensor as this may have been achieved at the expense of an unrealistic degree of scaling of the measurements. Even though we accepted the fact that there was some error introduced into the measured stress tensor by the use of an incorrect Young's modulus, there are limits to how much scaling would be realistic to compensate for this error. Scaling factors with large deviations from 1.0 would indicate additional and unknown sources of error. The negative value of D for site 1-2 of the Sub-6 region and a zero value for one additional site were two such unphysical results. These two sites were rejected from further analysis.

To investigate the measurement scaling factor results in more detail, we examined the distribution of D values, shown in Fig. 5. Since we were primarily concerned with incorrect scaling of the older (pre-1993) measurements, the histogram was restricted to the D values of those measurements. The D values have a mean of 0.8, median of 0.7 and the form of Fig. 6 is strongly suggestive of a normal distribution. It would appear, therefore, that the corrected Young's modulus applied to the pre-1991 measurements was still low since the mean value of D is less than 1.0. Since we have criteria for neither a distinct value of D nor magnitude of error value to serve as a cutoff point for accepting or rejecting a measurement result, all data (except for the two points with unphysical D values) were used for further analyses.

The magnitudes of the far-field tectonic stress tensor components are computed as the product of the unit response tensor coefficient and the magnitude of the

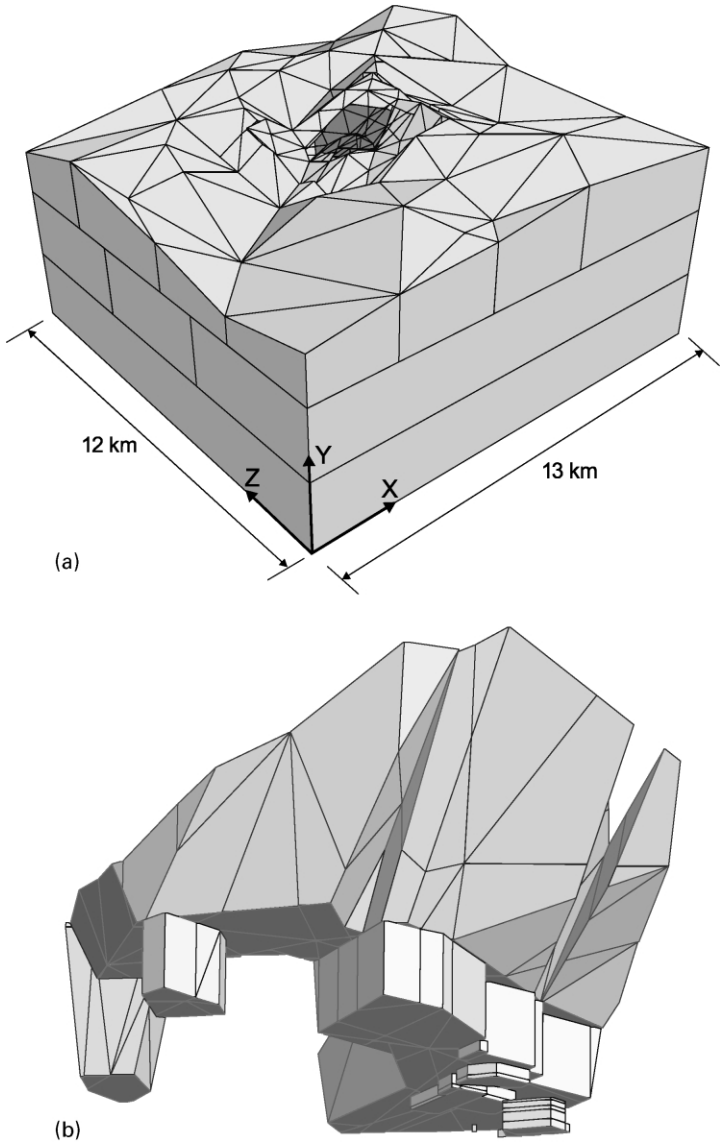

Fig. 5. Perspective views of 3DEC model of mine showing (a) regional model viewed from the southwest and (b) geometry of caved regions of the mine viewed from below and from the southeast. The dark shaded area in the central region of (a) shows the upper surface of caving shown in (b), and is approximately 2 km in span.

corresponding unit traction that was applied to the model boundary. In these models, normal tractions of magnitude −1 MPa and a shear traction of +1 MPa were used. The Cartesian and the corresponding principal components of the far-field tectonic stresses are shown in Table 3. The entire data set showed scatter in orientation and magnitude of the principal stresses similar to that shown in Table 3. If the mine had been in a single stress domain, then the magnitude and orientation of the far-field tectonic stress tensors would be similar for each measurement. Since this is clearly not the case at El Teniente, how can we further characterize the stress field?

It is important at this point to note the difference between the mine and its numerical representation. Some fairly extensive approximations were made in constructing the model, of which the greatest liberties were in representing the shear zones as regions of contrasting material properties. Also, all faults were omitted, and a simple method of initializing the stress field in the model was used. If, in these circumstances, the analysis had resulted in uniform far-field tectonic stress tensors, it would have indicated that the features omitted from the models were not important with respect to the stress field in the mine. The large variation in the tectonic component of the far-field stresses between measurement points indicated that important factors had been omitted from the model. This does not negate the utility of the model or the use of the analysis results. For practical purposes, model calibration is still necessary. The task is to identify domain boundaries and to characterize the stress field within those domains. A good basis for comparison when searching for domains is to compute the average far-field tectonic stresses using all measurements.

Table 2
Results of scaled measurement analysis of tectonic stress

Location	Site	Unit response tensor coefficients				Error value	Error tensor = estimated tectonic − computed tectonic					
		A	*B*	*C*	*D*	R^2	σ_x	σ_z	σ_y	τ_{xz}	τ_{xy}	τ_{yz}
Sub-6	1-2	−158.6	−36.6	47.8	−9.4	302.0	−2.0	2.7	9.5	−6.0	−11.5	5.7
	2-1	3.7	20.3	0.0	0.7	107.0	−1.4	−2.0	2.2	2.3	−9.3	2.3
	2-2	15.7	43.1	2.6	1.0	98.8	−3.1	−0.4	0.9	2.6	−5.4	7.3
	3-1	15.0	7.5	5.3	0.4	7.8	0.2	−0.2	1.1	−0.3	0.2	−2.5
	3-3	5.1	6.0	7.0	0.4	19.6	0.0	−0.1	2.0	−0.6	2.4	−3.1
	4-1	20.4	21.5	1.0	0.9	12.4	0.2	−0.3	0.9	0.1	−3.4	−0.1
	4-2	6.1	8.7	0.8	0.7	10.8	0.2	−0.4	1.0	0.1	−2.9	−1.1
	12-1	21.0	28.2	12.1	1.0	33.6	0.1	−0.6	4.0	−0.2	1.0	−4.1
	12-2	19.9	25.9	9.7	1.0	24.9	0.2	−0.9	2.7	−0.3	−2.1	−3.5
	6	7.4	12.1	5.8	0.6	38.0	−0.2	−0.4	2.6	−0.3	5.2	−1.9
	8	37.1	42.9	4.7	1.2	63.0	−1.2	0.4	1.0	−1.5	4.3	6.3
	9	27.4	20.4	2.9	0.9	24.5	−0.7	0.5	0.4	0.2	−4.1	2.6
	16	−4.5	7.6	2.2	0.3	12.1	−0.4	0.3	−0.3	−0.3	−0.5	3.4
	18	9.9	13.8	2.5	0.5	5.2	−0.3	0.2	−0.4	−0.2	0.2	2.2
	23	11.6	9.0	4.2	0.9	56.2	0.0	−0.1	2.2	−1.4	6.9	−1.1
	39	4.6	12.0	2.8	0.6	4.5	0.1	−0.1	0.4	−0.3	1.9	−0.8
	41	5.9	6.5	6.5	0.6	17.0	0.2	−0.2	1.5	0.1	−0.9	−3.7
	42	2.2	5.3	−1.4	1.5	240.0	−3.6	0.1	5.4	1.4	−7.1	12.1
	43	8.4	9.7	−1.0	0.4	23.4	−0.2	0.6	1.2	−0.4	−4.5	−1.0
	44	31.0	26.4	1.6	1.1	65.0	−0.0	−0.5	4.8	0.1	2.1	−6.1

5.4. Calculation of the average far-field tectonic stresses for the entire data set

The solution scheme can be adapted to determine the best-fit far-field tectonic stress tensor to the entire data set by changing the minimization objective function to be the average of the error values of all measurements. The results of this calculation are shown in Table 4. In this calculation, scaling coefficients *D* computed from the individual measurement analysis were used, since the scaling coefficient has a physical significance for each measurement.

As shown in Table 4, the major principal axis of the average far-field tectonic stress tensor is oriented almost exactly N–S. This is the same orientation as the shortening

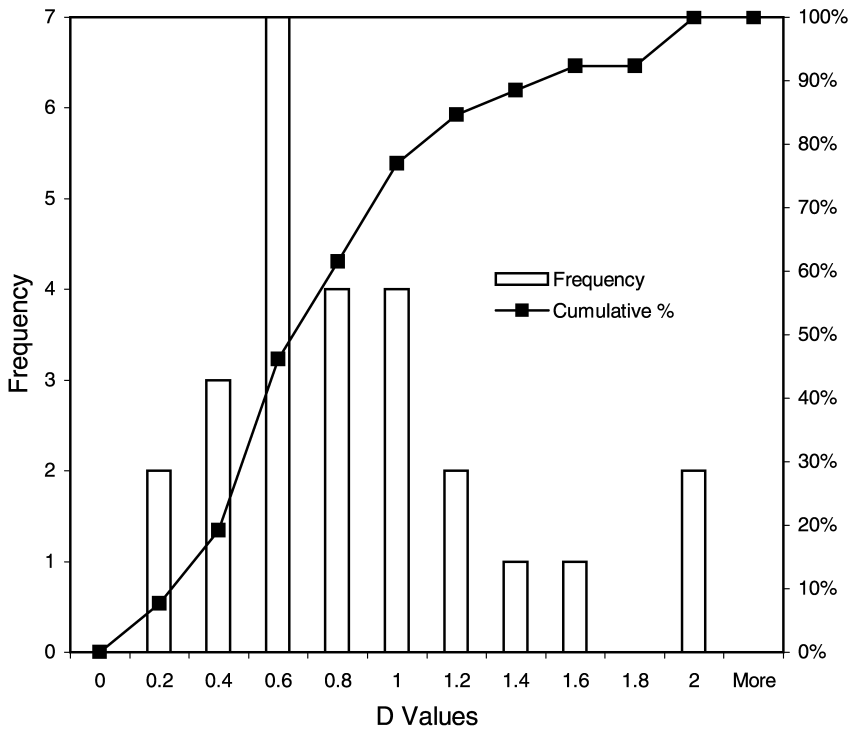

Fig. 6. Distribution of computed measurement scaling factor *D* for the pre-1991 measurements.

Table 3
Computed far-field tectonic stresses

Location	Site	Cartesian stresses			Principal stresses			
		σ_x	σ_z	τ_{xz}	σ_H	Trend	σ_h	Trend
Sub-6	2-1	−3.7	−20.3	0.0	−20.3	180.0	−3.7	90.0
	2-2	−15.7	−43.1	2.6	−43.3	174.7	−15.5	84.7
	3-1	−15.0	−7.5	5.3	−17.7	117.2	−4.8	27.2
	3-3	−5.1	−6.0	7.0	−12.5	136.7	1.4	46.7
	4-1	−20.4	−21.5	1.0	−22.1	150.3	−19.8	60.3
	4-2	−6.1	−8.7	0.8	−9.0	163.9	−5.8	73.9
	12-1	−21.0	−28.2	12.1	−37.2	143.3	−11.9	53.3
	12-2	−19.9	−25.9	9.7	−33.0	143.6	−12.8	53.6
	6	−7.4	−12.1	5.8	−16.0	146.0	−3.5	56.0
	8	−37.1	−42.9	4.7	−45.5	150.7	−34.4	60.7
	9	−27.4	−20.4	2.9	−28.5	109.6	−19.3	19.6
	6	4.5	−7.6	2.2	−8.0	169.8	4.9	79.8
	18	−9.9	−13.8	2.5	−15.0	153.9	−8.6	63.9
	23	−11.6	−9.0	4.2	−14.7	126.6	−5.9	36.6
	39	−4.6	−12.0	2.8	−13.0	161.6	−3.7	71.6
	41	−5.9	−6.5	6.5	−12.7	136.3	0.3	46.3
	42	−2.2	−5.3	−1.4	−5.9	20.8	−1.7	110.8
	43	−8.4	−9.7	−1.0	−10.2	27.8	−7.9	117.8
	44	−31.0	−26.4	1.6	−31.5	107.6	−25.9	17.6

axis of the most recent episode of deformation, as opposed to the E–W orientation that would be expected on the basis of the regional tectonics. The error values resulting from this average tensor fit were significantly higher than for the individually fit tensors. However, rejection of poorly fitting points from the calculation process resulted in very little change to either the average error value or the orientation and magnitude of the far-field tectonic stress tensor. This average fitting tensor serves as a benchmark with which to compare smaller groups of measurements.

5.5. Search for stress domains by grouping measurement points

For stability analysis purposes and to understand the physical basis for these stress field variations, we wished to search for domain boundaries using groups of measurements whose average error values were acceptably smaller than that of the entire data set but not significantly larger than those of individual measurements. The simplest starting point was to group measurements by physical proximity, or mining region.

The grouping of measurement sites by mining region is shown in Table 1. Eq. (4) was used in computing a single set of coefficients A, B, C for measurements in each group, together with individually calculated scaling coefficients D.

Table 4
Average far-field tectonic stress tensor for entire data set

	Magnitude (MPa)	Trend
σ_H	−15.8	4.1
σ_h	−10.2	94.1

The results of this calculation are summarized in Table 5. The average error value increases with the number of points in the group, and the Sub-6 region has a higher error value than the average of the entire data set even though it contains a much smaller number of points. This indicates that there is no strong correlation between stress field and region. It also indicates that stress domain boundaries most likely cut the area defined by mining regions.

The far-field tectonic stress tensors can also be compared in graphical format. Fig. 7 shows the principal stress tensors scaled relative to a circle with diameter of 20 MPa. The orientations appear to fluctuate around the mean N–S direction, but there is considerable scatter in the magnitudes and ratios of principal stresses. More meaningful groupings were sought based on geological characteristics. Since stress measurements are generally not available on a dense pattern throughout a mine, physically identifiable domain boundaries would be very useful. There has been considerable discussion in the literature about the effect of shear zones,

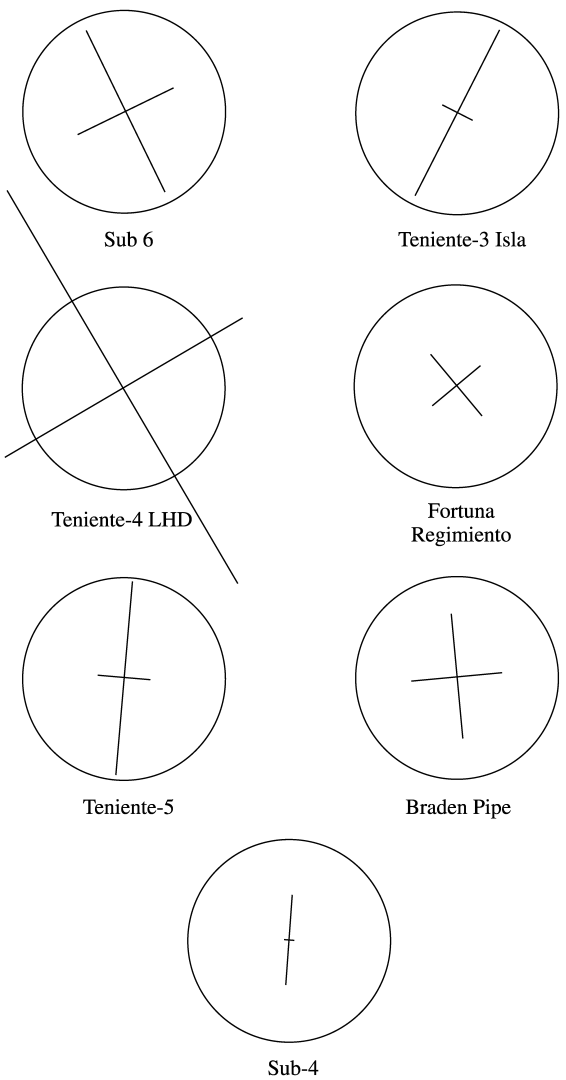

Fig. 7. Far-field tectonic stress tensors computed by region. Diameter of circles is 20 MPa.

Table 5
Average far-field tectonic stresses computed by region

Region	σ_H	Trend	σ_h	Trend	Error value	# Points
Sub-6	−17.6	154.6	−10.2	64.6	546	19
Ten-3 Isla	−19.2	27.4	−6.8	117.4	417	11
Ten-4 LHD	−45.0	149.6	−27.1	59.6	421	5
Fortuna/Regimiento	−8.3	140.2	−6.1	50.2	100	5
Ten-5	−19.1	4.9	−5.1	94.9	334	3
Pipe	−12.4	174.7	−8.9	84.7	164	3
Sub-4	−8.9	8.7	−1.0	98.7	60	2
All points	−15.8	4.1	−10.2	94.1	527	48

shear bands, localizations or faults on reorientation of a stress field (e.g. Vermeer and de Borst, 1984; Cundall, 1989; Hobbs et al., 1990; Vermeer, 1990; McKinnon and Garrido de la Barra, 1998), which provides a sound physical basis for using structural discontinuities to define stress domain boundaries. A shear zone is a strain localization within which the strength of the rock mass is lower than outside the zone, due to higher fracture frequency, and since the strength of the rock mass has been exceeded, shear stress levels within the zone should be lower than outside. This occurs through a reduction in the principal stress magnitudes and a rotation of the principal axes. The wide shear zones at El Teniente were therefore identified as candidates for defining domain boundaries.

Four groups of measurements were formed on the basis of structural characteristics. The results of the far-field tectonic stress analysis for these groups are shown in Table 6, and in graphical format in Fig. 8. These groups show lower mean error values than those grouped by region, with the exception of the group of measurement sites in shear zone intersections, which has an extremely high mean error value. The range of principal stress magnitudes is much smaller than the region groups shown in Table 5 and Fig. 7, but the orientation of the principal axes in each structural domain varies significantly. In a similar manner to the region groups, the orientation appears to fluctuate around a N–S direction.

Unfortunately, as with the grouping by region, the number of points constituting the groups is relatively small, rendering standard statistical tests of questionable value. Another simple way to compare these results is to examine how the mean error value changes with the number of points in each group. This is shown in Fig. 9. For reference, the dashed line in the figure corresponds to the mean error value for the entire data set. The results for structurally defined groups and mining region groups are quite different. The structural groups shows a decreasing mean error value with increasing number of points and a significantly smaller mean error value than either the region group or the entire data set. The structural group corresponding to shear zone intersections has relatively few points but has a very high mean error value, indicating that the group cannot be well represented by a single far-field tectonic stress tensor. Intersections appear to be characterized by highly irregular stress fields. The higher degree of fracturing and structural anisotropy in the intersections has a pronounced effect on scattering the stress field orientation. It is also noteworthy that measurement points forming each structural group are not necessarily located close together, lending stronger weight to the argument that structural domain grouping as opposed to location grouping is a more significant descriptor of the stress field. Since structural domains can be mapped, they form a convenient basis on which to characterize the stress field.

6. Geological interpretation of the measurements

The shear zones in the mine have gradational boundaries and the abrupt boundaries depicted in Fig. 1 are only approximate. These boundaries also meander vertically. Regions designated as being outside of shear zones still contain fractures associated with the shear zone but at a much lower fracture frequency. We also know from an analysis of kinematic indicators in the mine (Garrido et al., 1994), that there have been at least two episodes of deformation, the youngest of which had its shortening axis approximately N–S, consistent with the approximately

Table 6
Average far-field tectonic stresses, grouped by geology

Region	σ_H	Trend	σ_h	Trend	Error value	# Points
Outside shear zones	−16.3	38.0	−6.9	128.0	251	11
NE fault zone	−18.5	145.0	−8.0	55.0	251	12
NW fault zone	−13.1	8.0	−7.7	98.0	389	8
Intersections	−13.7	3.0	−9.5	93.0	1183	6
All points	−15.8	4.1	−10.2	94.1	527	48

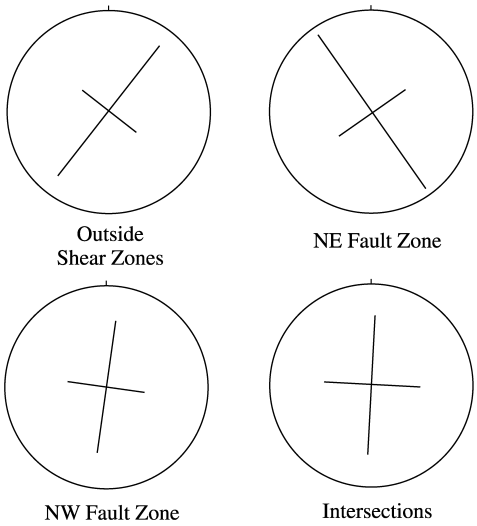

Fig. 8. Far-field tectonic stress tensors computed by structural domain grouping. Diameter of circles is 20 MPa.

N–S principal axis of the computed far-field tectonic stress tensor. While this may indicate that the shortening is still active, we cannot be certain because the current stress field magnitude may be below the critical threshold required to induce crustal shortening. We will show how the stress measurement data can be used to assess whether or not the TFZ is participating in regional deformation.

Since the kinematic analysis indicated that the existing discontinuity fabric was reactivated to accommodate crustal shortening in the most recent episode of deformation, the structures participating in the activity should have some influence on the orientation and magnitude of the stress field. If the structures were not correlated with the stress field, then we would not have found the grouping of measurements by structural domain to be as good a predictor as it was. If the structures are slipping, or close to the point of slip, the shear stress resolved on those structures should be at or close to the strength limit. This possibility was examined by plotting the measured major principal stress against minor principal stress, shown in Fig. 10, as these components of the stress field determine whether or not shear failure will take place. Data shown in this figure correspond to measured stresses scaled by the computed scaling factor D. Linear regression of the stress data produced a correlation coefficient of 0.75, indicating that the linear relationship is not unreasonable.

The rock mass strength was estimated by defining an envelope bounding the stress data, since the state of stress in a rock mass should always be below its strength. This envelope, also shown in Fig. 10, was set at 10 MPa above the regression line. This envelope corresponds to a Mohr–Coulomb cohesion of 2.4 MPa and friction angle of 20°. These values are in the range appropriate for a weak rock (Hoek and Brown, 1980). Changes in the position of the envelope parallel to the regression line would affect only the value of cohesion. The choice of 10 MPa was somewhat arbitrary and it can be seen in the figure that a number of points lie above the envelope. However, exact strength parameters are not the issue; it is the existence of a limiting

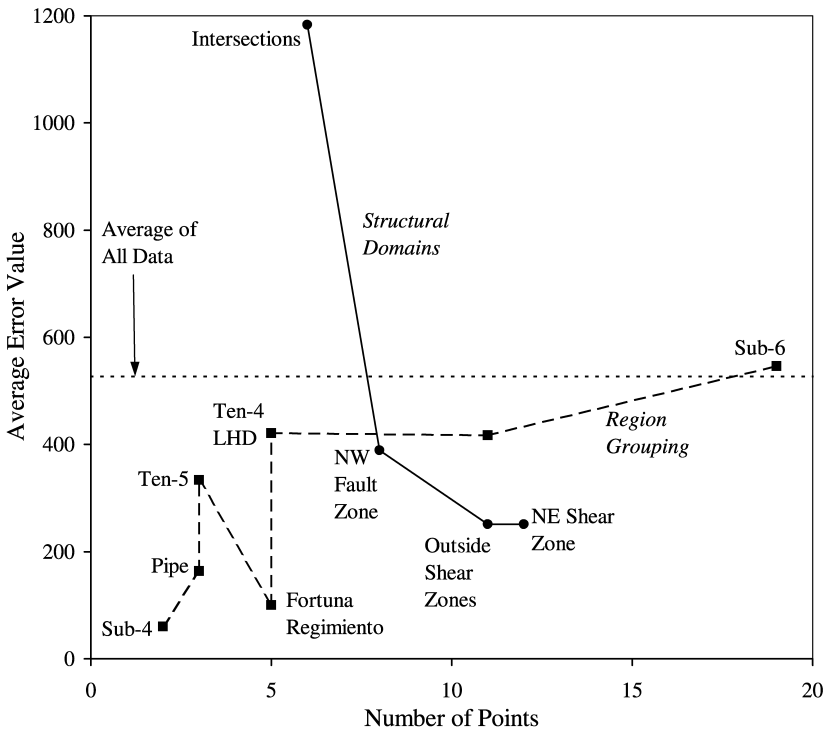

Fig. 9. Variation of computed error values with number of points in data set for measurement groupings by region and by structural domain. Average of all data is shown for reference.

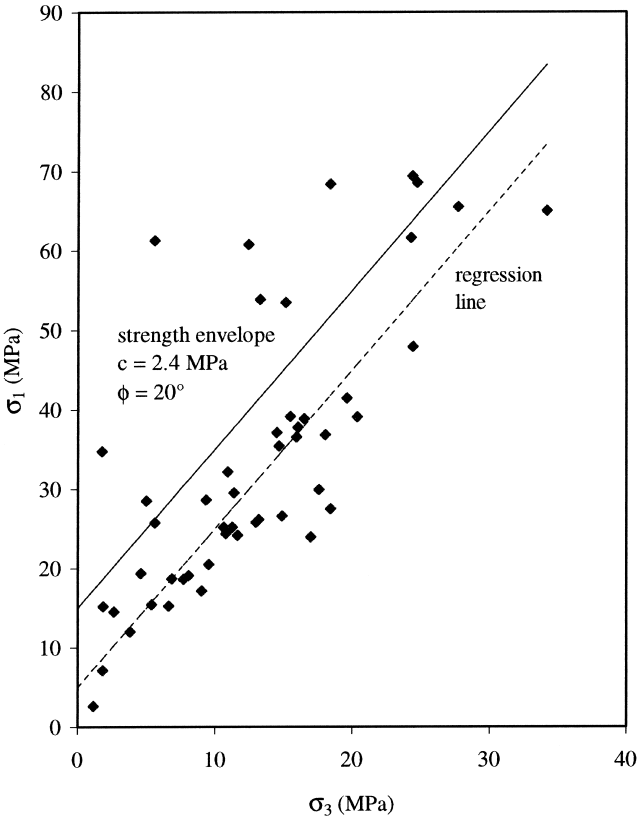

Fig. 10. Scaled stress measurement results showing envelope-like limit. Outlier points above the envelope are located in stronger rock types.

rock mass strength defined by the stress measurements that is most significant.

Examination of the data points lying above the strength envelope showed that they were all located in diorite, porphyry or outside of shear zones and hence were located in stronger rock types. Our interpretation of these 'higher strength' points is that they represent states of stress that can be tolerated by more competent material and do not reflect any limiting state of stress at the measurement point due to the strength of nearby structural discontinuities. This apparent limiting strength to the mine-scale rock mass is also interpreted as support for the hypothesis that the TFZ is an active regional tectonic structure, since there is a strong indication that it is in a state of marginal stability.

To check whether the mine-scale rock mass strength deduced from the stress measurements yielded meaningful values, we examined other indicators of large-scale rock strength. An independent numerical back-analysis of rock mass strength using microseismic data from the Sub-6 region of the mine, yielded Mohr–Coulomb cohesion values between 1.1 and 2.0 MPa and friction angles between 21 and 26°. The back-analysis procedure was based on a comparison of the numerically computed stress field at the location of the microseismic event with a strength value that would produce an excess shear stress drop consistent with the observed event magnitude. While these values represent dynamic strength they are in the same low range as the estimate from the stress measurement data. On an even larger scale, Jamison and Cook (1980) used stress drops from earthquake data to show that crustal strengths are similar to granular material with almost zero cohesion and a friction angle of approximately 30°. The low mine-scale rock mass strength deduced from the stress measurements is therefore not without precedent.

7. Discussion

Stress measurements are generally considered to be point measurements (Leijon, 1989) and yet collectively they have been shown to contain information about the rock mass on a much larger scale. This finding is relevant to our interpretation of the TFZ from a geological perspective, and to our interpretation of the stress field in the mine for engineering purposes. An additional question arising from these results is how generally can stress measurements be used to estimate rock mass strength?

In terms of rock mass behavior, we might expect the apparent limiting equilibrium state of regions within the TFZ to result in sensitivity to changes in stress brought about by mining, which would induce seismicity. The characteristics of self-organized critical systems (Bak and Tang, 1989; Sornette and Sornette, 1989; Rundle et al., 2000) imply that these events would not necessarily locate close to mining activity. A study of high quality microseismic events at the mine for which the moment tensor solutions were available, showed compatibility between slip vector orientations and the N–S oriented tectonic stress field (see Gephart (1990) for a description of the seismic moment tensor stress inversion method). For this to occur the mining induced component of the total stress field at the event sites must have been small, otherwise spatial stress gradients would have negated the assumption of constant stress in the source region. Source locations confirmed that these events did not occur close to mining activity. It appears, therefore, that at least some seismicity in the mine could have been the result of interaction between stress changes induced by mining and sensitive structures within the TFZ. It is not unprecedented that large engineering operations can induce seismic events (e.g. seismicity associated with reservoir filling; Grasso, 1993). We speculate on the basis of the stress measurement analysis results, in conjunction with certain characteristics of seismicity at the mine, that the TFZ is part of such a critical state system on a regional scale.

7.1. Use of stress measurements to estimate rock mass strength

Can spatially extended sets of stress measurement points be used to estimate large-scale rock mass strength? It appears to have been possible at the El Teniente Mine specifically because of its location in a tectonically active

portion of the crust. If the structural features constituting the fabric of the rock mass within which the mine is located are yielding, even if at a geological time scale, a relationship between the stress field and the strength of the rock mass would be expected. In regions that are not tectonically active or that are not sufficiently homogenized by faults connected to the regional scale, this relationship may not exist. Evidence for this was the stress measurements made in higher strength intrusions, whose stress state laid above the general strength envelope established for the rock mass at the mine.

7.2. Differences between regional and mine-scale stress field orientation

On the basis of horizontal principal stress indicators compiled as part of the World Stress Map Project (Zoback, 1992) we expected a predominantly E–W direction for the major principal axis of the far-field tectonic stress tensor. Evidence from (i) stress measurements, (ii) kinematic analysis of shear slip displacement indicators, and (iii) moment tensor analysis of microseismic data, all indicated an approximately N–S major principal stress axis of the horizontal components of the stress field in the mine i.e. perpendicular to the regional trend. Although geological evidence supported our findings, we were unable to establish a mechanical link between mine-scale and regional-scale structures to account for this local deviation. It is safe to say, however, that orebody mineralization occurs specifically because of local geological complexities. It is not surprising, therefore, that the stress field within this world-class mineral deposit does not conform to the regional trend. A study of stress measurements in the Mediterranean region (Rebaï et al., 1992) concluded that stress domains are defined by structures on different scales, i.e. large structures define large domains of stress, but within these domains, smaller domains of stress may be defined by sub-structures. This theme is consistent with the results of our analyses at the El Teniente Mine.

8. Conclusions

- Due to the significant influence of mining and topographically-induced stresses on the measured stresses, it was not possible to directly compare the measurements in order to characterize the stress field in the mine. The analysis procedure used provided a means of making a comparison possible. Calculation of the far-field tectonic stress tensor (non-gravitational horizontal boundary tractions) for each measurement point, which excludes all gravitational and locally induced effects, provided a rational means of comparing the stress field characteristics throughout the mine.
- Certain trends were seen in the orientation and magnitude of individually calculated far-field tectonic stress tensors but they also showed considerable scatter, even for closely spaced measurements. Tensor fits to measurement data grouped by location showed considerable scatter in both magnitude and orientation. The best grouping of measurements was shown to occur using geologically defined boundaries based on the location of shear zones cutting through the mine. Although the shear zones were not explicitly included in the numerical model (except as zones of differing material properties) they appear to have a major influence on the stress field in the mine.
- The computed far-field tectonic stress tensors for different structural domains had similar magnitudes but different orientations. The orientation of the major principal axes were scattered around an approximately N–S direction. This direction is orthogonal to the E–W orientation that would have been expected on the basis of regional tectonics. The best-fit far-field tectonic stress tensor for the entire data set also had its major principal axis oriented N–S. It is apparent that the El Teniente Fault Zone, within which the mine is located, is part of a structural system that has had a significant effect in modifying the regional stress field to that which occurs in the mine. Corroboration of this orientation using stress field orientations computed from high quality microseismic data and kinematic analysis of structural data indicated that this discrepancy between the orientation of the regional and mine-scale stress field is not an artifact of the stress measurement analysis technique, although the reason for this discrepancy is currently unknown.
- When plotted in principal stress space, the stress measurements showed an envelope-like trend, which indicated that the stress levels in the mine were to some extent controlled by a large-scale strength limit. While the strength computed from this envelope was low, it was consistent with strengths computed from microseismic event magnitude data. This was interpreted to imply that, on a large scale, the shear zones in the mine, and probably the El Teniente Fault Zone, are currently active in accommodating tectonically driven deformation. On a large scale, the shear zones must be at or close to a state of limiting equilibrium with tectonic driving forces.
- The strength envelope suggested by the measurements is considerably lower than the rock mass strength derived from rock mass classification, implying significant scale dependent strength and rock mass behavior at the mine. This is attributed to the size of the mine being sufficient to interact with regional scale geological structures, which influence the apparent strength. Smaller excavations do not interact with large-scale structures and therefore have a higher apparent strength.

Acknowledgements

The data was analyzed as part of the Proyecto Geodinámico (API-11689), sponsored by CODELCO

Chile, Division El Teniente. The authors gratefully acknowledge the sponsorship of the mine. Support of the project by Jorge Quiroga (Superintendente General GeologÍa) and Daniel Trivelli (Subgerente General de Operaciones) is acknowledged. Pedro Varona and Jonny Sjöberg are recognized for their stimulating discussion as the method was being developed and for assisting with portions of the analysis. Two anonymous reviewers are thanked for their comments that have helped improve the content and focus of the paper.

References

Bak, P., Tang, C., 1989. Earthquakes as self-organized critical phenomenon. Journal of Geophysical Research 94 (B11), 15,635–15,637.

Brown, E.T., Hoek, E., 1978. Trends in relationships between measured in-situ stresses and depth. International Journal of Rock Mechanics and Mining Sciences 15, 211–215.

Cundall, P.A., 1989. Numerical experiments on localization in frictional materials. Ingenieru-Archiv 59, 148–159.

Duncan Fama, M.E., Pender, M.J., 1980. Analysis of the hollow inclusion technique for measuring in situ rock stress. International Journal of Rock Mechanics and Mining Sciences 17, 137–146.

Garrido, I., Riveros, M., Cladouhos, T., Espiñeira, D., Allmendinger, R., 1994. Modelo geológico estructural yacimiento El Teniente: 7° Congreso Geológico Chileno, Concepción. v. II, pp. 1553–1558.

Garrido, I., Cembrano, J., Siña, A., Stedman, P., Yánez, G., 2002. High magma oxidation state and bulk crustal shortening: key factors in the genesis of Andean prophyry copper deposits, central Chile (31–34°). Revista Geologica de Chile 29(1) 43–54.

Gephart, J., 1990. Stress and the direction of slip on fault planes. Tectonics 9 (4), 845–858.

Grasso, J.R., 1993, Triggering of self-organized system: implications for the state of the uppermost crust. In: Young R.P. (Ed.), Rockbursts and Seismicity in Mines, Balkema, Rotterdam, 187–194.

Herget, G., 1987. Stress assumptions for underground excavations in the Canadian Shield. International Journal of Rock Mechanics and Mining Sciences 24, 95–97.

Hobbs, B.E., Mülhaus, H.-B., Ord, A., 1990. Instability, softening and localization of deformation. In: Knipe, R.J., Rutter, E.H. (Eds.), Deformation, Rheology and Tectonics. Geological Society Special Publication 54, pp. 143–165.

Hoek, E., Brown, E.T., 1980. Underground Excavations in Rock, The Institution of Mining and Metallurgy, London.

Hoek, E., Brown, E.T., 1997. Practical estimates of rock mass strength. International Journal of Rock Mechanics and Mining Sciences 34, 1165–1186.

ISRM Commission on Testing Methods, 1987. Suggested methods for rock stress determination. International Journal of Rock Mechanics and Mining Sciences 24, 53–73.

Itasca Consulting Group, Inc., 1994. 3DEC Version 1.5. Itasca Consulting Group, Inc., Minneapolis, Minnesota.

Jamison, D.B., Cook, N.G.W., 1980. Note on measured values for the state of stress in the earth's crust. Journal of Geophysical Research 85 (B4), 1833–1838.

Kvapil, R., Baeza, J., Flores, G., 1989. Block caving at El Teniente mine, Chile. Transactions of the Institution of Mining and Metallurgy, Section A 98, 43–56.

Lavenu, A., Cembrano, J., 1999. Compressional and transpressional stress pattern for Pliocene and Quaternary brittle deformation in fore arc and intra-arc zones (Andes of Central and Southern Chile). Journal of Structural Geology 21, 1669–1691.

Leijon, B.A., 1989. Relevance of pointwise rock stress measurements—an analysis of overcoring data. International Journal of Rock Mechanics and Mining Sciences 26, 61–68.

Maksaev, V., Munizaga, F., Michael, M., Fanning, M., Mathur, R., Ruiz, J., Thiele, K., 2002. El Teniente porphyry copper deposit in the Chilean Andes: new geochronological timeframe and duration of hydrothermal activity. 2002 Denver Annual Meeting (October 27–30, 2002) Session no. 152—Booth# 4 Economic Geology (Posters). Geological Society of America.

Marrett, R., Allmendinger, R.W., 1990. Kinematic analysis of fault-slip data. Journal of Structural Geology 12, 973–986.

McKinnon, S.D., 2001. Analysis of stress measurements using a numerical model methodology. International Journal of Rock Mechanics and Mining Sciences 38, 699–709.

McKinnon, S.D., Garrido de la Barra, I., 1998. Fracture initiation, growth and effect on stress field: a numerical investigation. Journal of Structural Geology 20 (12), 1673–1698.

Microsoft Corporation, 1999. Excel 2000.

Pan, E., Amadei, B., Savage, W.Z., 1994. Gravitational stresses in long symmetric ridges and valleys in anisotropic rock. International Journal of Rock Mechanics and Mining Sciences 31, 293–312.

Ramos, V.A., Aguirre-Urreta, M.B., Alvarez, P.P., Cegarra, M.I., Cristallini, E.O., Kay, S.M., Lo Forte, G.L., Pereyra, F.X., Perez, D.J., 1996. Geología de la Región del Aconcagua, Anales No. 24, Dirección Nacional del Servicio Geológico, Subsecretaria de la Nación, Buenos Aires, Argentina, p. 510.

Rebaï, S., Philip, H., Taboada, A., 1992. Modern tectonic stress field in the Mediterranean region; evidence for variation in stress directions at different scales. Journal of Geophysical Research 109, 1–35.

Rojas, E., Cuevas, J., Barrera, V., 1992. Analysis of the Wear in Drawpoint Brows at El Teniente Mine, Massmin 92, South African Institution of Mining and Metallurgy, Johannesburg.

Rundle, J.B., Turcotte, D.L., Klein, W. (Eds.), 2000. GeoComplexity and the Physics of Earthquakes. American Geophysical Union Geophysical Monograph no. 120.

Sanderson, D., Marchini, R.D., 1984. Transpression. Journal of Structural Geology 6, 449–458.

Savage, W.Z., 1993. Gravity induced stresses near a vertical cliff. International Journal of Rock Mechanics and Mining Sciences 30, 325–330.

Savage, W.Z., Swolfs, H.S., 1986. Tectonic and gravitational stress in long symmetric ridges and valleys. Journal of Geophysical Research 91, 3677–3685.

Sornette, A., Sornette, D., 1989. Self-organized criticality and earthquakes. Europhysics Letters 9 (3), 197–202.

Tassara, A., Yañez, G., 1997. Segmentación de los Andes (12–50°S): un punto de vista reológico aportado por un análisis flexural: 8° Congreso Geológico Chileno. v. I, p. 271.

Timoshenko, P.S., Goodier, J.N., 1970. Theory of Elasticity, McGraw-Hill, New York.

Vermeer, P.A., 1990. The orientation of shear bands in biaxial tests. Géotechnique 40, 223–236.

Vermeer, P.A., de Borst, R., 1984. Non-associated plasticity for soils, concrete and rock. Heron 29, 1–63.

Zoback, M.L., 1992. First- and second-order patterns of stress in the lithosphere; the World Stress Map Project. Journal of Geophysical Research 97 (B8), 11,703–11,728.